
Going with the Speed of Sound: Pushing Neural Surrogates into Highly-turbulent Transonic Regimes

Fabian Paischer^{*1,2}, Leo Cotteleer^{*1}, Yann Dreze^{*1}, Richard Kurle^{*1}, Dylan Rubini¹,
Maurits Bleeker¹, Tobias Kronlachner¹, Johannes Brandstetter^{1,2}

¹ Emmi AI GmbH, Linz

² ELLIS Unit, Institute for Machine Learning, JKU Linz

Abstract

The widespread use of neural surrogates in automotive aerodynamics, enabled by datasets such as DrivAerML and DrivAerNet++, has primarily focused on bluff-body flows with large wakes. Extending these methods to aerospace, particularly in the transonic regime, remains challenging due to the high level of non-linearity of compressible flows and 3D effects such as wingtip vortices. Existing aerospace datasets predominantly focus on 2D airfoils, neglecting these critical 3D phenomena. To address this gap, we present a new dataset of CFD simulations for 3D wings in the transonic regime. The dataset comprises volumetric and surface-level fields for around 30,000 samples with unique geometry and inflow conditions. This allows computation of lift and drag coefficients, providing a foundation for data-driven aerodynamic optimization of the drag-lift Pareto front. We evaluate several state-of-the-art neural surrogates on our dataset, including Transolver and AB-UPT, focusing on their out-of-distribution (OOD) generalization over geometry and inflow variations. AB-UPT demonstrates strong performance for transonic flowfields and reproduces physically consistent drag-lift Pareto fronts even for OOD wing configurations. Our results highlight its potential as an efficient and effective tool for rapid aerodynamic design exploration. To facilitate future research, we open-source our dataset at <https://huggingface.co/datasets/EmmiAI/Emmi-Wing>.

1 Introduction

Machine learning-based surrogates have recently emerged as powerful tools for accelerating aerodynamic design and analysis [1, 2]. In automotive aerodynamics, large-scale datasets such as DrivAerML [3] and DrivAerNet++ [4, 5] have enabled neural models to predict complex bluff-body flows with remarkable accuracy, potentially reducing reliance on expensive Computational Fluid Dynamics (CFD) simulations. In aerospace applications, the design goals and flow physics differ significantly from the automotive domain. Automobiles are bluff bodies with early flow separation, leading to high pressure drag [6]. In contrast, aircrafts are streamlined bodies designed to maintain attached flow and optimize the lift-to-drag ratio [7], which we refer to as drag-lift Pareto front.

While CFD is a fundamental design tool, its high computational cost creates a bottleneck in the design cycle. This has spurred the development of data-driven surrogate models [8, 1, 9, 10, 11, 12, 13, 14, 15, 16], which learn the complex mapping between geometry and flow fields [17]. However, extending these approaches to aerospace applications remains challenging. Transonic flight regimes involve intricate 3D phenomena, such as shock-boundary layer interactions and wingtip vortices, that are not captured with existing 2D airfoil datasets [18, 19, 20, 21]. Moreover, the lack of publicly

*Equal contribution

available high-fidelity 3D flow data limits the development and benchmarking of neural surrogates capable of generalizing across realistic aircraft geometries and operating conditions, as well as optimizing lift-to-drag performance.

To address these limitations, we introduce a new dataset of high-fidelity RANS simulations for 3D wings in the transonic regime. To the best of our knowledge, this is the first publicly available dataset that comprehensively captures both geometric and inflow variations for realistic 3D configurations. The dataset comprises approximately 30,000 simulations with a unique combination of geometry and inflow parameters, providing volumetric as well as surface-level flow-field data. These data enable the computation of aerodynamic performance metrics such as lift, drag, and drag–lift polars, thereby supporting data-driven design-space exploration and optimization.

Using our new dataset, we evaluate several state-of-the-art neural surrogates, including Transolver [9] and the recently proposed AB-UPT [1], with a focus on out-of-distribution generalization to unseen geometries and flow conditions. Our results show that AB-UPT accurately predicts transonic flow fields and can reproduce physically consistent lift–drag trade-offs for unseen configurations, outperforming all competitors. Overall, our study demonstrates that AB-UPT can approximate lift–drag Pareto fronts for unseen geometries, highlighting its potential as practical tool for rapid aerodynamic design exploration.

2 Methodology

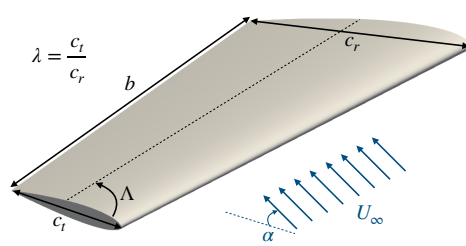
Our methodology centers on the generation of a high-fidelity dataset of 3D wings operating in the transonic regime, followed by the evaluation of state-of-the-art neural surrogate models. Existing aerospace CFD datasets predominantly focus on subsonic 2D airfoils, as summarized in Table 1, and therefore neglect critical 3D flow phenomena such as shock–boundary layer interactions and wingtip vortices. We generate a new dataset comprising around 30,000 cases with a unique combination of geometry and inflow parameters. The data generation process is organized into three key components: (i) the design of experiments for geometry and flow conditions, (ii) the setup and execution of high-fidelity CFD simulations, and (iii) the dataset split strategy used for training and evaluating neural surrogates.

Table 1: Comparison of publicly available aerodynamic CFD datasets for machine learning.

Dataset	Size	Dim.	Regime	Notes
AirFRANS [18]	~1 000	2D	Subsonic	ML benchmark, varied AoA/Re
UniFoil [19]	500 K	2D	Sub-/Transonic	Very large 2D dataset, wide Re/Mach range
AirFoilCFD [20]	~18 K	2D	Subsonic	9k shapes, 2 AoA, fixed inflow
AirFoilML [21]	2 600	2D	Subsonic	NACA airfoils, fixed AoA/Re
BlendedNet [22]	~10 K	3D	Subsonic	Blended wing-body, 9 flight conds.
Emmi-Wing (Ours)	~30 K	3D	Sub-/Transonic	30K unique geometries + inflows, drag/lift polars

CFD setup. We conduct simulations using the open-source CFD solver, OpenFOAM-v2506 [23]. The steady-state, compressible flow rhoSimpleFoam solver [24] is used for all cases using the perfect gas assumption. For turbulence modeling, we selected the Spalart-Allmaras model which offers good computational efficiency and robust convergence for transonic wing flows with predominantly attached boundary layers, despite the presence of weak-to-moderate shocks [25]. Spatial discretization utilized second-order schemes including a van Leer limiter for momentum and a bounded upwind scheme for energy/pressure terms, with first-order upwind differencing applied to turbulence quantities for enhanced stability. The wing surfaces are set with a no-slip condition, and freestream conditions are applied at the far-field boundaries. The angle of attack is imposed via the inflow boundary condition rather than by altering the wing geometry. The meshing process relies on OpenFOAM’s built-in snappyHexMesh to generate a high-quality, body-fitted mesh. Prismatic boundary layer meshing is used to achieve low y^+ values in the range [50 – 200] in all cases. We verify our CFD setup using empirical data from wind tunnel measurements of the OneraM6 wing at different angles of attack [26, 27].

Design of experiments. We select a 2D NACA0012 airfoil profile, which is extruded into 3D based on four geometric parameters: the span (b), the taper ratio (λ), the sweep angle (Λ), and the root



Parameter	Range	
c_r	[0.7, 1.2]	m
b	[1.0, 1.5]	m
λ	[0.4, 0.7]	–
Λ	[0.0, 40.0]	deg
U_∞	[150, 300]	m/s
α	[-10, 10]	deg
M	[0.43, 0.87]	–
Re	[5.14, 19.4]e6	–

Figure 1: A visual representation of the parameterized 3D wing geometry alongside the four key geometric design parameters and the two inflow condition parameters with their respective sampling ranges used for the design of experiments. The geometry parameters include the span (b), taper ratio (λ), sweep angle (Λ), and chord root (c_r); inflow parameters are the inflow velocity (U_∞) and angle of attack (α); dimensionless parameters are mach number (M) and Reynolds number (Re).

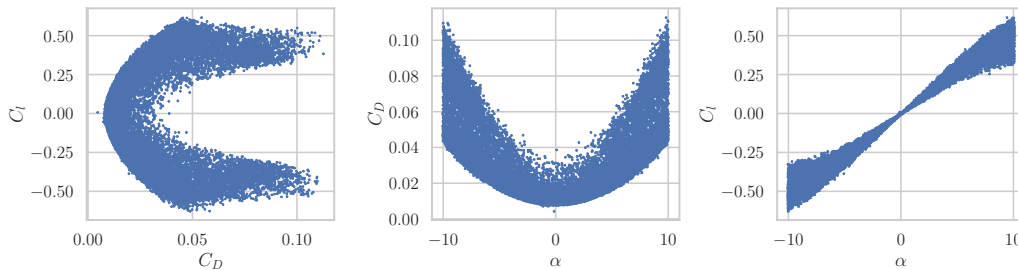


Figure 2: **Left:** Pareto frontier of drag C_D versus lift C_l coefficients for all cases in the dataset. **Middle:** C_D as a function of angles of attack present in the dataset. **Right:** C_l as a function of the angles of attack present in the dataset.

chord (c_r). In addition, we vary two inflow parameters, namely velocity (U_∞) and angle of attack (α). To ensure a broad and diverse range of flow conditions, a total of 29,727 unique simulation cases were created by randomly sampling each of the six variables from a uniform distribution within a application-relevant predefined range. The specific ranges for each parameter and their visual representation are depicted in Figure 1.

The resulting dataset comprises 29,727 cases, including both surface and volumetric data. The surface data consists of pressure p_s and wall shear-stress τ on the wing. The volumetric data contains the full 3D flow field, including pressure p_v , the velocity vector $\mathbf{u} = [u_x, u_y, u_z]$, its magnitude $\|\mathbf{u}\|$, and the vorticity vector $\boldsymbol{\omega} = [\omega_x, \omega_y, \omega_z]$ and its magnitude $\|\boldsymbol{\omega}\|$ at each point of the CFD mesh. We provide visualizations of the lift-to-drag Pareto front as well as drag/lift coefficients over varying angles of attack for all cases in Figure 2. In addition we visualize a set of 3D wing geometries for the minimum and maximum of each parameter in Figure 14 in the Appendix. Finally, Figure 3 shows a representative sample for a transonic sample of our dataset exhibiting flow detachment at high angles of attack and the formation of turbulent structures at the wingtip.

Dataset split. We partition the dataset into a training, a validation, and three test sets, including two in-distribution (ID) sets and one out-of-distribution (OOD) set. The two ID sets are designed as (i) **random selection**: a random selection of 1,000 cases within the convex hull of the training set, and (ii) **interpolation**: a parameter region within the convex hull of the parameter space that spans 1,000 unseen cases. The former evaluates in-distribution performance, while the latter specifically targets the ability of the surrogate to interpolate between cases in an unseen ID parameter region. The 1,000 OOD cases are selected as the outermost points of the convex hull of the parameter space. To create the OOD set and the ID interpolation set, where we used an iterative convex hull peeling method and isolate the 1,000 outermost data points and the 1,000 innermost points, respectively. The remaining 25,727 cases are used for training.

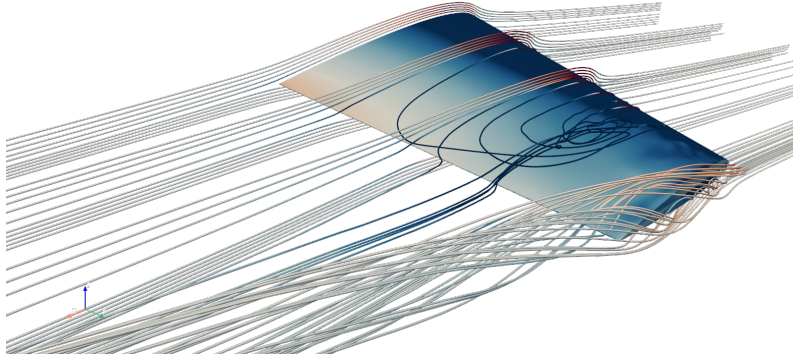


Figure 3: 3D effects on wing.

Additional parameter scans. Practitioners are usually concerned with the optimization of the drag–lift Pareto front. To this end, lift and drag coefficients are usually investigated on parameter scans of various angles of attack α and varying wing geometries to obtain the wing geometry resulting in the highest lift and lowest drag forces. To assess the ability of neural surrogate models to capture these coefficients for different parameter scans we run additional cases with a unique geometry ($c_r = 0.806$, $b = 1.1963$, $\lambda = 0.562$) that does not occur in the 29,727 cases. We run two parameter sweeps for this geometry, namely (i) $\alpha \in \{-30, -28, \dots, 28, 30\}$, and (ii) $\Lambda \in \{0, 10, 20, 30, 40, 50, 60, 70\}$, to evaluate in-distribution and OOD generalization. The latter sweep concerns a geometry parameter (sweep angle) as it is the geometry parameter apart from AoA with the most impact on lift/drag. This results in another 248 cases solely used for evaluation.

3 Experiments

We conduct a series of experiments to evaluate the generalization capabilities of state-of-the-art neural surrogate models trained on our 3D transonic wing dataset. Our analysis focuses on two main aspects: (i) the in-distribution performance of different architectures on flowfield and aerodynamic coefficient prediction, and (ii) their out-of-distribution generalization to unseen geometries and inflow conditions.

Neural surrogates. We benchmark four neural surrogate models on our dataset: PointNet [28], Transolver [9], AB-UPT [1], and a Vision Transformer [29]. To incorporate inflow conditions and geometry design parameters, we add their embeddings to the input for PointNet, and for the transformer-based models we use a conditioning as in Diffusion Transformers [30]. All models are trained with a Mean Squared Error (MSE) loss applied to all fields for three different seeds.

Evaluation. We evaluate the predictive performance using the pointwise relative L_2 error, which is normalized by the L_2 norm of the ground truth. In addition, we report the coefficient of determination (R^2) between drag/lift coefficients obtained from the best surrogate model with the ground truth coefficients. Finally, we provide drag–lift Pareto fronts for parameter scans of the best performing surrogate model compared to ground truth to stress-test their generalization ability.

Results. We report results for volume and surface-level quantities in Table 2 for the different methods. As expected we observe a consistent increase of error the more the model is pushed towards an OOD evaluation regime across all neural surrogate models. Furthermore, our results show that except for PointNet, all surrogate approaches perform similarly on surface-level quantities. However, on volume-level quantities that exhibit high variance, like vorticity, AB-UPT shows a significant improvement over competitors. Therefore, we consider AB-UPT the strongest neural surrogate approach and evaluate it on the different parameter scans.

We provide a qualitative analysis of the AB-UPT model on the OOD test set. Figure 8 in the Appendix shows pressure and friction profiles of a randomly sampled test case of the OOD set at a normalized

Table 2: Mean and standard deviation of relative L2 errors for surface fields (p_s , τ) and volume fields (p_v , \mathbf{u} , ω) of different neural surrogates across three seeds.

Test Set	Model	p_s	τ	p_v	\mathbf{u}	ω
Interpol	PointNet	0.052 \pm 0.0005	0.227 \pm 0.0005	0.050 \pm 0.0000	0.152 \pm 0.0010	0.238 \pm 0.0050
	Transformer	0.002 \pm 0.0000	0.022 \pm 0.0000	0.002 \pm 0.0000	0.011 \pm 0.0000	0.071 \pm 0.0005
	Transolver	0.002 \pm 0.0000	0.022 \pm 0.0000	0.002 \pm 0.0000	0.011 \pm 0.0000	0.090 \pm 0.0022
	AB-UPT	0.002 \pm 0.0000	0.022 \pm 0.0009	0.002 \pm 0.0005	0.010 \pm 0.0008	0.064 \pm 0.0043
ID	PointNet	0.101 \pm 0.0000	0.441 \pm 0.0020	0.096 \pm 0.0000	0.299 \pm 0.0005	0.374 \pm 0.0015
	Transformer	0.005 \pm 0.0005	0.042 \pm 0.0005	0.005 \pm 0.0000	0.034 \pm 0.0005	0.102 \pm 0.0000
	Transolver	0.005 \pm 0.0000	0.042 \pm 0.0005	0.005 \pm 0.0000	0.034 \pm 0.0005	0.119 \pm 0.0017
	AB-UPT	0.006 \pm 0.0009	0.042 \pm 0.0026	0.006 \pm 0.0009	0.035 \pm 0.0031	0.094 \pm 0.0066
OOD	PointNet	0.120 \pm 0.0000	0.582 \pm 0.0040	0.115 \pm 0.0005	0.398 \pm 0.0010	0.475 \pm 0.0000
	Transformer	0.008 \pm 0.0000	0.057 \pm 0.0009	0.007 \pm 0.0005	0.051 \pm 0.0005	0.125 \pm 0.0005
	Transolver	0.007 \pm 0.0005	0.055 \pm 0.0005	0.007 \pm 0.0005	0.051 \pm 0.0009	0.142 \pm 0.0024
	AB-UPT	0.008 \pm 0.0008	0.057 \pm 0.0043	0.008 \pm 0.0014	0.051 \pm 0.0040	0.116 \pm 0.0093

span location $y/b = 0.75$. The corresponding 3D visualizations of the true surface fields, the predicted fields, and the prediction errors are shown in Figure 4. Remarkably, both pressure coefficient (C_p) and friction coefficient (C_f) match the ground truth closely. Another interesting observation is that surface friction (C_f) exhibits non-physical streaks on the wing surface. Upon further investigation, we find that these artifacts are of numerical nature and non-physical. Even though such artifacts may be present in the dataset, AB-UPT seems not to be affected by them and still predicts a smooth surface friction field and the prediction error clearly shows that these artifacts are not captured. We attribute this to the inherent bias of neural networks towards low-frequency components [31] since the numerical artifacts mainly consist of high-frequency components. Ultimately, this resembles another instance in which a neural surrogate potentially surpasses a numerical simulation due to inductive biases, first observed in [32]. In addition, it highlights the potential of AB-UPT acting as anomaly detector for data curation and removal of high-frequency numerical artifacts.

In Figure 5 we report correlation of drag C_D and lift C_l coefficients with the ground truth for all cases in the OOD test set. The predictions of AB-UPT align closely with the ground-truth coefficients ($R^2 = 1.0$ for C_l and $R^2 = 0.998$ for C_D). Furthermore we report the error distribution across cases in the OOD test set for different combinations of drag and lift in Figure 11. Intriguingly, we find that AB-UPT is most error-prone in high C_D regimes, which are dominated by errors in τ and rather far from the tangent on the lift-drag Pareto front. This highlights that AB-UPT is a promising contender for wing design optimization.

Parameter scans. We evaluate AB-UPT on the parameter scans that comprise 248 simulations with sweeps over Λ and α with the remaining parameters fixed. We report correlation of the predicted values for C_l and C_D in Figure 5c and 5d, respectively, with highlighted cases for out-of-range (OOR) values of α and Λ . Remarkably, AB-UPT maintains high correlation with the ground-truth ($R^2 = 0.911$ for C_l , $R^2 = 0.804$ for C_D) even when observing values that are far beyond the range of values for α or Λ it has been trained on. We complement this observation with relative errors for surface quantities p_s and τ , as well as an average thereof in Figure 12. Interestingly, AB-UPT seems to perform better for positive angles of attack than for negative ones, even though the dataset was sampled uniformly between them.

In addition, we report the predicted drag-lift Pareto fronts for a selected set of sweep angles ($\Lambda \in \{20, 40, 50, 70\}$) and compare them to the ground-truth in Figures 6 and 7. Intriguingly, we observe minor deviations from the ground truth for values up to $\alpha \sim 20^\circ$, which is far beyond the range the model has been trained on. Furthermore, the tangent on the drag-lift Pareto front is well captured up to $\Lambda = 50$, which is again out-of-range compared to the training set. For larger $\Lambda > 50$ we observe larger divergence from the ground-truth. Finally, we report pressure coefficient C_p and friction coefficient C_f at a normalized span length of $y/b = 0.5$ for a test case with out-of-range $\alpha = 20^\circ$ and sweep angle $\Lambda = 40$. We also show C_p and C_f for the full 3D wing in Figures 10a and 10b, respectively.

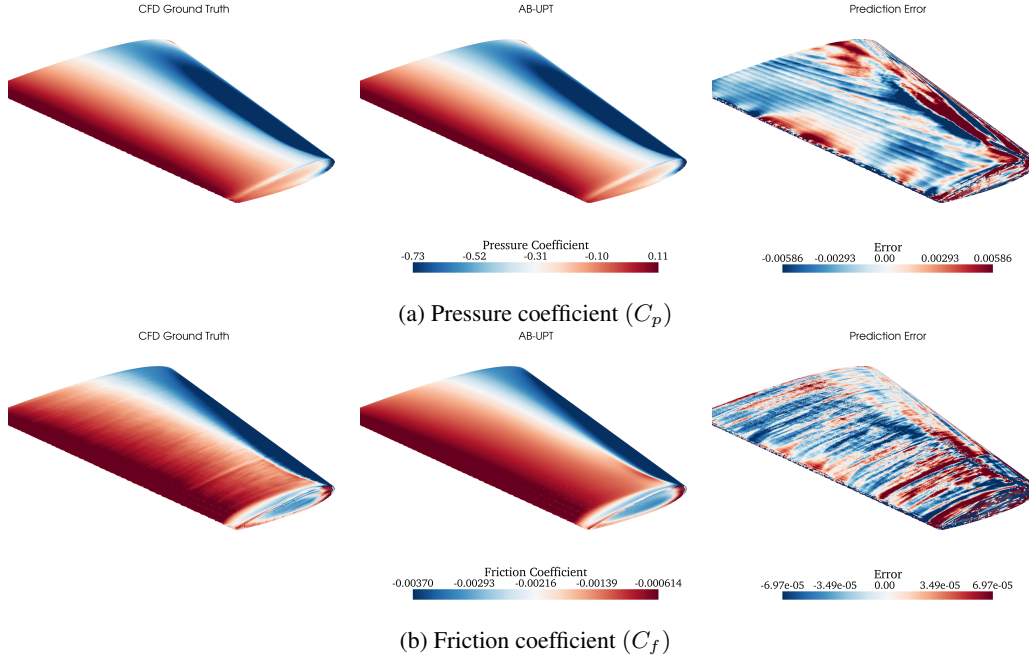


Figure 4: Comparison between surface field coefficients on the wing’s surface of the CFD (left), AB-UPT surrogate (center) and the error between them (right). The case presented is from the extrapolation test set with geometry and inflow conditioning parameters within the training range.

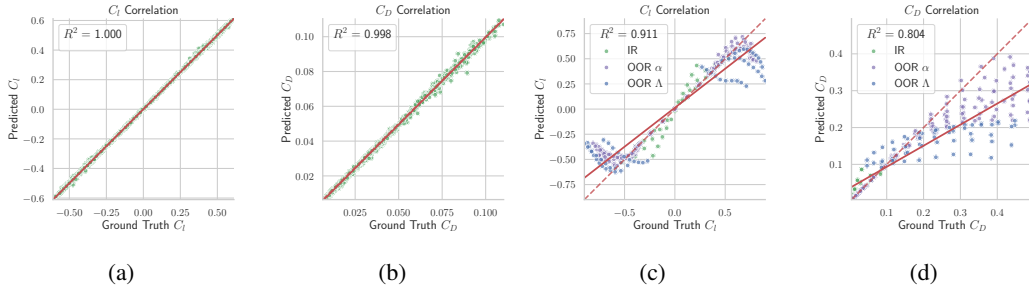


Figure 5: Correlation of predicted C_l (5a) and C_D (5b) from AB-UPT to the ground truth for all cases in the OOD test set. AB-UPT’s predictions closely match the ground truth. Figures 5c and 5d depict correlation of C_l and C_D to ground-truth for all cases in the parameter scans with out-of-range parameters highlighted. AB-UPT still produces highly correlated results.

Design Optimization. There are two avenues of performing design optimization, namely (i) CFD-based optimization [33, 34, 35], and (ii) data-driven surrogate-based optimization [36, 37, 38, 39]. The former typically employs adjoint methods [40, 41] combined with gradient-based optimizers, requiring the repeated solution of the governing PDE system. Traditional surrogate-based approaches instead usually construct low-dimensional response surfaces to predict quantities of interest directly from design parameters, significantly reducing computational cost but limiting physical fidelity. Our AB-UPT directly operates on the physical fidelity of the CFD simulation, while bypassing the need to solve the governing PDE system.

We utilize our dataset to demonstrate how AB-UPT can be used for rapid design exploration and optimization. This requires real-time generation of new geometries from the design parameters in a suitable format that can be processed by the model, since the optimization explores new designs. Furthermore, gradient-based design optimization methods require the geometry generation to be differentiable. Relying on the traditional simulation meshes (e.g., taking cell centers as inputs)

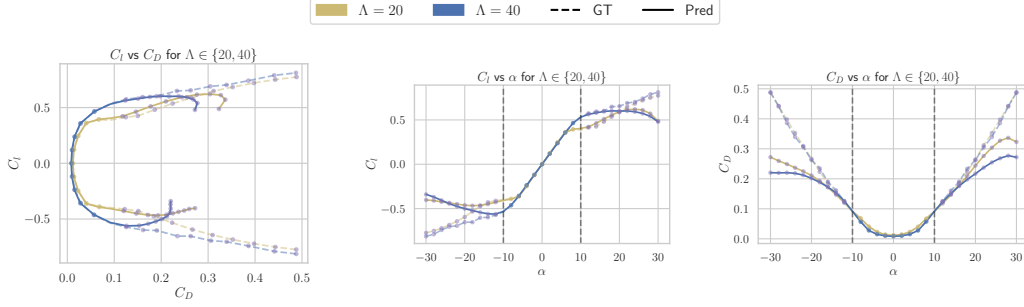


Figure 6: Ground-truth vs predicted C_l and C_D for parameter scans over $\alpha \in \{-30, \dots, 30\}$ and $\Lambda \in \{20, 40\}$. Out-of-range cases are highlighted by purple markers, and the ground-truth is represented as dashed line. AB-UPT reproduces the drag-lift Pareto front well (left), but introduces error in high regimes of $\alpha > 20$ for both C_l (middle) and C_D (right).

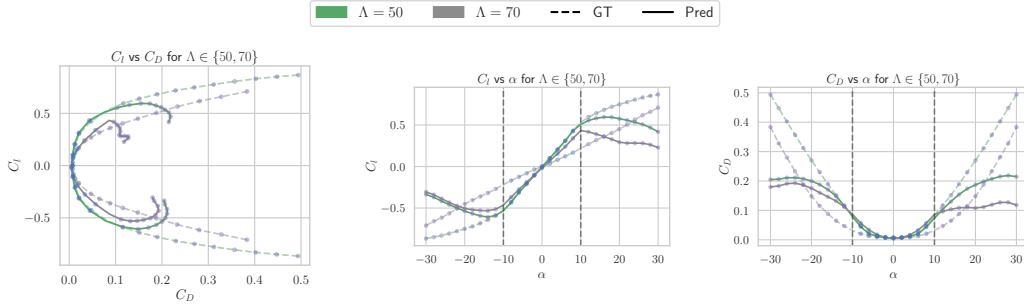


Figure 7: Ground-truth vs predicted C_l and C_D for parameter scans over $\alpha \in \{-30, \dots, 30\}$ and $\Lambda \in \{50, 70\}$. Out-of-range cases are highlighted by purple markers, and the ground-truth is represented as dashed line. AB-UPT reproduces the drag-lift Pareto front for the most part (left), but error accumulates especially for higher values of α and $\Lambda = 70$ for both C_l (middle) and C_D (right).

prohibits this workflow, as the meshing process is computationally intensive and generally not differentiable.

To address this problem, we train AB-UPT to take a computer-aided-design (CAD) representation as input to the geometry encoder and the anchor tokens (cf. Section 4.6 in [1]). Specifically, we generate stereolithography (STL) data in a fully differentiable manner and at arbitrary resolution by lofting a parametric NACA0012 profile along the wing span, applying affine transformations defined by the root chord, taper ratio, and sweep angle. This enables the generation of meshes for arbitrary wing configurations in milliseconds, enabling continuous design exploration.

The cell centers of a low resolution STL mesh serve as input to the AB-UPT geometry encoder and surface anchor tokens, while cell centers from a higher resolution mesh serve as query tokens to predict higher-fidelity surface fields from which we can derive aerodynamic coefficients such as lift and drag. We compute the drag and lift coefficients according to Eq. 2 for a particular mesh and use the lift-to-drag ratio $\varepsilon = C_D/C_l$ as a measure of aerodynamic efficiency. Finally, we formulate the optimization problem as $\max_{\phi} \varepsilon$, where the design vector $\phi = \{c_r, b, \lambda, \Lambda, U_{\infty}, \alpha\}$ comprises the four geometry parameters and two inflow conditions. Note that while we consider optimizing both geometry and inflow conditions, it is straightforward to define a constrained optimization problem such as optimizing the geometry for a specific cruise flight speed.

We explore three optimization methods, (i) gradient-based optimization (Adam [42]), (ii) evolutionary strategies (CMA-ES [43, 44]), and (iii) Bayesian optimization (Gaussian Process [45]). We initialize each method with parameter values in the center of the training data range and bound the search space to the training range. Each method is run for 2 minutes on an H100 GPU until convergence and the resulting parameters, as well as the corresponding aerodynamic coefficients, are summarized in Table 3. Notably, the gradient-based method converges to a different solution than the evolutionary

strategy and Bayesian optimization, with a distinct optimal flight speed, sweep angle, and angle of attack. We hypothesize that this behavior is due to the gradient-based approach being more prone to local optima. To validate the newly found solution, we identify its nearest neighbor in the training set and compare the corresponding lift-to-drag ratio. Indeed, we observe that the nearest neighbors in parameter space align well with the newly explored solutions. Remarkably, though, the explored solutions exhibit slightly higher lift-to-drag ratio, indicating that our design optimization loop found more efficient 3D wing configurations than present in the dataset it has been trained on. These results demonstrate the promise of leveraging neural surrogates for aerodynamic design optimization.

Table 3: Performance comparison of optimization methods, running each method for approximately 2 minutes. The model forward and backward (in case of gradient-based) is computed on an H100 GPU in float16 precision. The gradient-based methods finds a different optimum compared to the gradient-free methods with similar lift-to-drag ratio (ϵ) We compare the optima to the nearest neighbor in the dataset (NN) and also show the best parameter set in the dataset, which is the nearest neighbor of the solution found by the gradient-based method.

Method	# steps	Input parameters						Coefficients		
		c_r [m]	b [m]	λ	Λ [°]	U_∞ [m/s]	α [°]	C_d	C_l	ϵ
Gradient	900	0.704	1.499	0.401	33.03	150.1	5.060	0.0179	0.3281	18.36
Evolutionary	2700	0.701	1.498	0.401	39.96	209.0	4.746	0.0165	0.3040	18.43
Bayesian	100	0.700	1.500	0.400	40.00	212.4	4.664	0.0163	0.3002	18.43
Gradient (NN)	-	0.710	1.468	0.443	27.72	154.3	4.371	0.0160	0.2905	18.12
Evolutionary (NN)	-	0.750	1.487	0.435	39.67	232.9	3.723	0.0138	0.2395	17.34
Bayesian (NN)	-	0.750	1.487	0.435	39.67	232.9	3.723	0.0138	0.2395	17.34
Best ϵ in dataset	-	0.710	1.468	0.443	27.72	154.3	4.371	0.0160	0.2905	18.12

4 Discussion and Limitations

To the best of our knowledge we are the first to introduce a dataset of 3D wing geometries in the transonic regime and to show that neural surrogates can be used for aerodynamic design optimization. However, there are some shortcomings to our work, mainly related to the dataset generation process. Generally, we emphasize that there are many knobs to turn with respect to data generation that can lead to uncertainty in the resulting simulations, including mesh quality, turbulence-model assumptions, convergence criteria, and, importantly, solver fidelity. These effects are exacerbated when moving from the subsonic to the transonic regime, where severe shockwaves and turbulence occur. In this work we relied on OpenFOAM, as it is advantageous for accessibility and automation. Furthermore, our current study relies on relatively simple wing geometries (NACA0012-based) and steady-state RANS simulations to reduce the cost of data generation. As a result, inherent unsteady phenomena are not captured by the solver. Despite these factors, our results demonstrate that neural surrogates trained on our dataset retain significant practical value. They enable efficient exploration of drag-lift Pareto fronts and exhibit potential for anomaly detection.

5 Conclusion

We present a first comprehensive dataset of high-fidelity RANS simulations for 3D wings operating in the transonic regime. Each simulation case comes with unique geometry and inflow parameters and provides volume and surface-level flowfields. We evaluate state-of-the-art neural surrogates on our dataset and find that AB-UPT outperforms other state-of-the-art and provides strong performance even for unseen cases. Furthermore, we demonstrate that AB-UPT accurately reproduces drag-lift Pareto fronts even for cases with parameters far beyond its training regime, establishing itself as a contender for real-time wing geometry optimization.

In the future our aim is to investigate the use of neural surrogates for anomaly detection to provide an iterative data generation pipeline and ensure data curation. Furthermore, we plan to explore other numerical solvers and compare to empirical data if available. Finally, we aim to push the boundary of

efficiency such that our surrogates can be used as practical tool to explore the aerodynamic design space and optimize the lift-to-drag performance of unseen geometries in real time.

References

- [1] Benedikt Alkin, Maurits Bleeker, Richard Kurle, Tobias Kronlachner, Reinhard Sonnleitner, Matthias Dorfer, and Johannes Brandstetter. Ab-upt: Scaling neural cfd surrogates for high-fidelity automotive aerodynamics simulations via anchored-branched universal physics transformers, 2025.
- [2] Benedikt Alkin, Richard Kurle, Louis Serrano, Dennis Just, and Johannes Brandstetter. Ab-upt for automotive and aerospace applications. *arXiv preprint arXiv:2510.15808*, 2025.
- [3] Neil Ashton, Charles Mockett, Marian Fuchs, Louis Fliessbach, Hendrik Hetmann, Thilo Knacke, Norbert Schonwald, Vangelis Skaperdas, Grigoris Fotiadis, Astrid Walle, Burkhard Hupertz, and Danielle Maddix. Drivaerml: High-fidelity computational fluid dynamics dataset for road-car external aerodynamics, 2025.
- [4] Mohamed Elrefaie, Angela Dai, and Faez Ahmed. Drivaernet: A parametric car dataset for data-driven aerodynamic design and graph-based drag prediction. volume Volume 3A: 50th Design Automation Conference (DAC) of *International Design Engineering Technical Conferences and Computers and Information in Engineering Conference*, page V03AT03A019. Curran Associates, Inc., 08 2024.
- [5] Mohamed Elrefaie, Florin Morar, Angela Dai, and Faez Ahmed. Drivaernet++: A large-scale multimodal car dataset with computational fluid dynamics simulations and deep learning benchmarks. In A. Globerson, L. Mackey, D. Belgrave, A. Fan, U. Paquet, J. Tomczak, and C. Zhang, editors, *Advances in Neural Information Processing Systems*, volume 37, pages 499–536. Curran Associates, Inc., 2024.
- [6] Pijush K. Kundu and Ira M. Cohen. *Fluid mechanics / Pijush K. Kundu, Ira M. Cohen ; with contributions by P.S. Ayyaswamy and H.H. Hu*. Academic Press, Amsterdam ;, 4th ed. edition, 2008.
- [7] John D. Jr. Anderson. *Fundamentals of Aerodynamics*. McGraw-Hill Education, New York, 6th edition, 2017.
- [8] Benedikt Alkin, Andreas Fürst, Simon Schmid, Lukas Gruber, Markus Holzleitner, and Johannes Brandstetter. Universal physics transformers: A framework for efficiently scaling neural operators. *Advances in Neural Information Processing Systems*, 37:25152–25194, 2024.
- [9] Haixu Wu, Huakun Luo, Haowen Wang, Jianmin Wang, and Mingsheng Long. Transolver: A fast transformer solver for pdes on general geometries. In *International Conference on Machine Learning*, 2024.
- [10] Huakun Luo, Haixu Wu, Hang Zhou, Lanxiang Xing, Yichen Di, Jianmin Wang, and Mingsheng Long. Transolver++: An accurate neural solver for pdes on million-scale geometries, 2025.
- [11] Zongyi Li, Nikola B. Kovachki, Kamyar Azizzadenesheli, Burigede Liu, Kaushik Bhattacharya, Andrew M. Stuart, and Anima Anandkumar. Fourier neural operator for parametric partial differential equations. *CoRR*, abs/2010.08895, 2020.
- [12] Lu Lu, Pengzhan Jin, Guofei Pang, Zhongqiang Zhang, and George Em Karniadakis. Learning nonlinear operators via deeponet based on the universal approximation theorem of operators. *Nature Machine Intelligence*, 3(3):218–229, March 2021.
- [13] Zongyi Li, Nikola Borislavov Kovachki, Chris Choy, Boyi Li, Jean Kossaifi, Shourya Prakash Otta, Mohammad Amin Nabian, Maximilian Stadler, Christian Hundt, Kamyar Azizzadenesheli, and Anima Anandkumar. Geometry-informed neural operator for large-scale 3d pdes, 2023.
- [14] Zijie Li, Kazem Meidani, and Amir Barati Farimani. Transformer for partial differential equations’ operator learning. *Transactions on Machine Learning Research*, 2023.

- [15] Tobias Pfaff, Meire Fortunato, Alvaro Sanchez-Gonzalez, and Peter Battaglia. Learning mesh-based simulation with graph networks. In *International Conference on Learning Representations*, 2021.
- [16] Zongyi Li, Nikola Kovachki, Kamyar Azizzadenesheli, Burigede Liu, Kaushik Bhattacharya, Andrew Stuart, and Anima Anandkumar. Neural operator: Graph kernel network for partial differential equations. *arXiv preprint arXiv:2003.03485*, 2020.
- [17] Steven L. Brunton, Bernd R. Noack, and Petros Koumoutsakos. Machine learning for fluid mechanics. *Annual Review of Fluid Mechanics*, 52(Volume 52, 2020):477–508, 2020.
- [18] Florent Bonnet, Ahmed Jocelyn Mazari, Paola Cinnella, and Patrick Gallinari. Airfrans: High fidelity computational fluid dynamics dataset for approximating reynolds-averaged navier-stokes solutions, 2023.
- [19] Rohit Sunil Kanchi, Benjamin Melanson, Nithin Somasekharan, Shaowu Pan, and Sicheng He. Unifoil: A universal dataset of airfoils in transitional and turbulent regimes for subsonic and transonic flows, 2025.
- [20] Dakota Ramos, Andrew Glaws, Ryan King, Bumseok Lee, Olga Doronina, James Baeder, Ganesh Vijayakumar, and Zachary Grey. Airfoil computational fluid dynamics - 9k shapes, 2 aoa’s. Open Energy Data Initiative (OEDI), National Renewable Energy Laboratory (NREL), <https://doi.org/10.25984/2222587>, 2023. Accessed: 2025-10-30.
- [21] Alessandro Schillaci, Maurizio Quadrio, and Giacomo Boracchi. A database of cfd-computed flow fields around airfoils for machine-learning applications, 2021. Version 1.0.
- [22] Nicholas Sung, Steven Spreizer, Mohamed Elrefaie, Kaira M. Samuel, Matthew C. Jones, and Faez Ahmed. Blendednet: A blended wing body aircraft dataset and surrogate model for aerodynamic predictions. *CoRR*, abs/2509.07209, 2025.
- [23] H. G. Weller, G. Tabor, H. Jasak, and C. Fureby. A tensorial approach to computational continuum mechanics using object-oriented techniques. *Computer in Physics*, 12(6):620–631, 11 1998.
- [24] L. S. Caretto, A. D. Gosman, S. V. Patankar, and D. B. Spalding. Two calculation procedures for steady, three-dimensional flows with recirculation. In Henri Cabannes and Roger Temam, editors, *Proceedings of the Third International Conference on Numerical Methods in Fluid Mechanics*, pages 60–68, Berlin, Heidelberg, 1973. Springer Berlin Heidelberg.
- [25] OpenFOAM Wiki. Oneram6 by michael alletto — openfoam wiki,, 2024. [Online; accessed 12-November-2025].
- [26] V. Schmitt and Françoise Charpin. Pressure distributions on the onera m6 wing at transonic mach numbers. 1979.
- [27] M. Mani, J. Ladd, A. Cain, R. Bush, M. Mani, J. Ladd, A. Cain, and R. Bush. *An assessment of one- and two-equation turbulence models for internal and external flows*. 1997.
- [28] Charles Ruizhongtai Qi, Hao Su, Kaichun Mo, and Leonidas J. Guibas. Pointnet: Deep learning on point sets for 3d classification and segmentation. In *2017 IEEE Conference on Computer Vision and Pattern Recognition, CVPR 2017, Honolulu, HI, USA, July 21-26, 2017*, pages 77–85. IEEE Computer Society, 2017.
- [29] Alexey Dosovitskiy, Lucas Beyer, Alexander Kolesnikov, Dirk Weissenborn, Xiaohua Zhai, Thomas Unterthiner, Mostafa Dehghani, Matthias Minderer, Georg Heigold, Sylvain Gelly, Jakob Uszkoreit, and Neil Houlsby. An image is worth 16x16 words: Transformers for image recognition at scale. In *ICLR*, 2021.
- [30] William S. Peebles and Saining Xie. Scalable diffusion models with transformers. *2023 IEEE/CVF International Conference on Computer Vision (ICCV)*, pages 4172–4182, 2022.
- [31] Damien Teney, Armand Mihai Nicolicioiu, Valentin Hartmann, and Ehsan Abbasnejad. Neural redshift: Random networks are not random functions. In *Proceedings of the IEEE/CVF Conference on Computer Vision and Pattern Recognition*, pages 4786–4796, 2024.

- [32] Felix Koehler and Nils Thuerey. Neural emulator superiority: When machine learning for pdes surpasses its training data. *arXiv preprint arXiv:2510.23111*, 2025.
- [33] Joaquim RRA Martins. Perspectives on aerodynamic design optimization. In *AIAA Scitech 2020 Forum*, page 0043, 2020.
- [34] Zhoujie Lyu, Gaetan K. W. Kenway, and Joaquim R. R. A. Martins. Aerodynamic shape optimization investigations of the common research model wing benchmark. *AIAA Journal*, 53(4):968–985, 2015.
- [35] Xiaolong He, Jichao Li, Charles A. Mader, Anil Yildirim, and Joaquim R.R.A. Martins. Robust aerodynamic shape optimization—from a circle to an airfoil. *Aerospace Science and Technology*, 87:48–61, 2019.
- [36] Jichao Li and Mengqi Zhang. Data-based approach for wing shape design optimization. *Aerospace Science and Technology*, 112:106639, 2021.
- [37] Jichao Li, Mengqi Zhang, Joaquim R. R. A. Martins, and Chang Shu. Efficient aerodynamic shape optimization with deep-learning-based geometric filtering. *AIAA Journal*, 58(10):4243–4259, 2020.
- [38] N. Bartoli, T. Lefebvre, S. Dubreuil, R. Olivanti, R. Priem, N. Bons, J.R.R.A. Martins, and J. Morlier. Adaptive modeling strategy for constrained global optimization with application to aerodynamic wing design. *Aerospace Science and Technology*, 90:85–102, 2019.
- [39] Abdelkader Benaouali and Stanisław Kachel. Multidisciplinary design optimization of aircraft wing using commercial software integration. *Aerospace Science and Technology*, 92:766–776, 2019.
- [40] Gaetan K.W. Kenway, Charles A. Mader, Ping He, and Joaquim R.R.A. Martins. Effective adjoint approaches for computational fluid dynamics. *Progress in Aerospace Sciences*, 110:100542, 2019.
- [41] Yayun Shi, Charles A. Mader, Sicheng He, Gustavo L. O. Halila, and Joaquim R. R. A. Martins. Natural laminar-flow airfoil optimization design using a discrete adjoint approach. *AIAA Journal*, 58(11):4702–4722, 2020.
- [42] Diederik P. Kingma and Jimmy Ba. Adam: A method for stochastic optimization. In *International Conference on Learning Representations (ICLR)*, 2015.
- [43] Nikolaus Hansen and Andreas Ostermeier. Completely derandomized self-adaptation in evolution strategies. *Evol. Comput.*, 9(2):159–195, June 2001.
- [44] Nikolaus Hansen. The cma evolution strategy: A tutorial, 2023.
- [45] Donald R. Jones, Matthias Schonlau, and William J. Welch. Efficient global optimization of expensive black-box functions. *Journal of Global Optimization*, 13:455–492, 1998.
- [46] Xiangning Chen, Chen Liang, Da Huang, Esteban Real, Kaiyuan Wang, Hieu Pham, Xuanyi Dong, Thang Luong, Cho-Jui Hsieh, Yifeng Lu, and Quoc V. Le. Symbolic discovery of optimization algorithms. In Alice Oh, Tristan Naumann, Amir Globerson, Kate Saenko, Moritz Hardt, and Sergey Levine, editors, *Advances in Neural Information Processing Systems 36: Annual Conference on Neural Information Processing Systems 2023, NeurIPS 2023, New Orleans, LA, USA, December 10 - 16, 2023*, 2023.
- [47] Jacob Devlin, Ming-Wei Chang, Kenton Lee, and Kristina Toutanova. BERT: pre-training of deep bidirectional transformers for language understanding. In Jill Burstein, Christy Doran, and Tamar Solorio, editors, *Proceedings of the 2019 Conference of the North American Chapter of the Association for Computational Linguistics: Human Language Technologies, NAACL-HLT 2019, Minneapolis, MN, USA, June 2-7, 2019, Volume 1 (Long and Short Papers)*, pages 4171–4186. Association for Computational Linguistics, 2019.

A Drag/Lift coefficients

In this section we provide a definition of the drag and lift coefficients, commonly used in aerospace engineering. Aerodynamic forces quantify interesting properties of a wing such as drag and lift, which are the result of an integration of the surface pressure p_s and friction $\boldsymbol{\tau}$, i.e., force per unit area exerted by the fluid on the surface, acting tangential (parallel) to the surface. These forces are obtained from the total force acting on an object in an airflow, which is given by

$$\mathbf{F} = \oint_S \left(- (p_s - p_\infty) \mathbf{n} + \boldsymbol{\tau} \right) dS, \quad (1)$$

where p_s is the surface pressure, p_∞ the free stream pressure, \mathbf{n} the surface normal vector, and $\boldsymbol{\tau}$ the contribution of friction. Drag and lift coefficients are defined as dimensionless numbers

$$C_D = \frac{2 \mathbf{F} \cdot \mathbf{e}_{\text{drag}}}{\rho v^2 A_{\text{ref}}}, \quad C_L = \frac{2 \mathbf{F} \cdot \mathbf{e}_{\text{lift}}}{\rho v^2 A_{\text{ref}}}, \quad (2)$$

and often used in engineering [3], where \mathbf{e}_{drag} is a unit vector into the free stream direction, \mathbf{e}_{lift} a unit vector into the lift direction perpendicular to the free stream direction, ρ the density, v the magnitude of the free stream velocity, and A_{ref} a characteristic reference area for a certain geometry. Further, the acting force \mathbf{F} can be converted into dimensionless numbers as drag and lift forces

$$\mathbf{F}_{\text{drag}} = \mathbf{F} \cdot \mathbf{e}_{\text{drag}}, \quad \mathbf{F}_{\text{lift}} = \mathbf{F} \cdot \mathbf{e}_{\text{lift}}. \quad (3)$$

When simulating an airplane in flight, the angle of attack α is a common boundary condition which changes free stream \mathbf{e}_{drag} and lift direction \mathbf{e}_{lift} as given by the unit velocity vector \mathbf{u}_∞ as

$$\mathbf{u}_\infty = \begin{bmatrix} \cos(\alpha) \\ 0 \\ \sin(\alpha) \end{bmatrix}, \quad \mathbf{e}_{\text{drag}} = \frac{\mathbf{u}_\infty}{\|\mathbf{u}_\infty\|_2}, \quad \mathbf{e}_{\text{lift}} = \mathbf{e}_{\text{drag}} \times \begin{bmatrix} 0 \\ 1 \\ 0 \end{bmatrix}, \quad (4)$$

where $\|\cdot\|_2$ is the Euclidian norm. For $\alpha = 0$ these reduce to $\mathbf{e}_{\text{drag}} = (1, 0, 0)$ and $\mathbf{e}_{\text{lift}} = (0, 0, 1)$.

B Implementation Details

We perform a hyperparameter search over learning rate $\text{lr} \in \{1e-5, 3e-5, 5e-5, 1e-4\}$ for all methods and select the best performing one. We train for 10 epochs with a learning rate of $1e-5$ with linear warmup for the first 5% of training and a cosine decay thereafter. We train in `float16` precision using the Lion optimizer [46] with a weight decay of $\lambda = 0.05$ and gradient clipping of 0.25. We preprocess the different fields using z-score normalization except for vorticity where we apply normalization by the average magnitude. We elaborate on the method-specific details for the different methods as follows.

AB-UPT. For AB-UPT we use a hidden dimension of 192 and set the number of anchor points for both volume and surface branches to 16, 384. Before processing the geometry we subsample it to 65, 536 points and perform supernode pooling to 16, 384 points. The hidden dimensionality is set to 192 and the total number of parameters for this model amounts to 7.1 million.

Transformer. We use a Transformer architecture based on coordinates encoded via continuous sine-cosine positional embeddings [47] and a hidden dimension of 192. We employ 16 Transformer blocks with three attention heads, resulting in a parameter count of roughly 7.4M parameters.

Transolver. The Transolver baseline integrates the attention mechanism from [9] into the Transformer baseline. We use 512 slices for the Transolver attention. The remainder of the architecture is the same as for the Transformer baseline, resulting in a parameter count of 7.5M parameters.

PointNet. We use a hidden dimension of 192 and an input embedding of 96. We use a global position embedding of 3072 dimensions, resulting in a model size of roughly 8.3M parameters.

C Ablation studies

Our dataset incorporates variations in geometric design parameters that are *observable* through the point cloud and *non-observable* inflow conditions (e.g., inflow Mach number). We therefore performed an ablation study on the best-performing model, AB-UPT, to assess the impact of conditioning

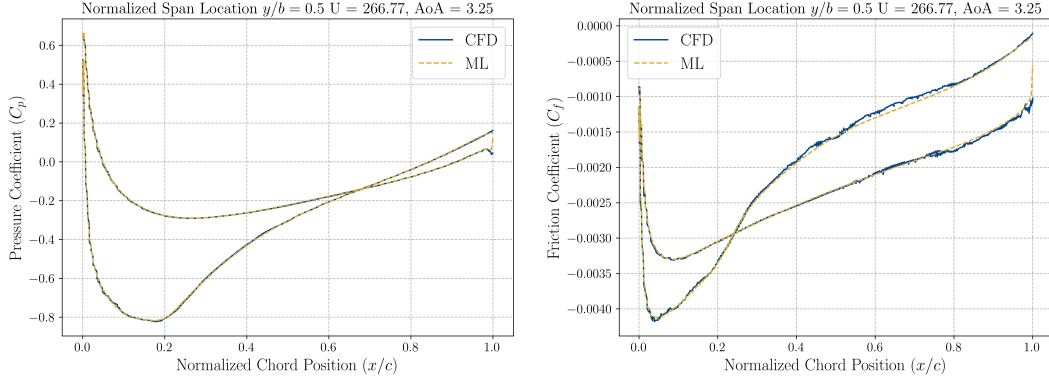


Figure 8: Comparison between CFD data (blue) and AB-UPT prediction (dashed yellow) for the pressure coefficient (C_p) and friction coefficient (C_f) on the wing surface at a normalized span location of $y/b = 0.5$ for a case of the OOD test set. 3D visualizations are shown in Figure 4.

on these parameters (relative L2 error, Table 4). The results demonstrate that the AB-UPT architecture effectively infers information about the geometry directly from the point cloud, while non-observable parameters like inflow conditions are required as explicit conditioning inputs.

Table 4: Impact of geometry and inflow conditioning on the AB-UPT surrogate model’s performance, measured by relative L2 error (%) on the *in-distribution* test set. All models were trained for 10 epochs.

Conditioning		Relative L2 error (%)				
Geometry	Inflow	p_s	τ	p_v	u	ω
✓	✓	0.53	4.16	0.49	3.36	10.5
✓	✗	0.54	4.16	0.51	3.42	10.6
✗	✓	10.8	43.5	9.58	29.5	33.7
✗	✗	10.9	43.7	9.59	29.6	34.3

D Additional results

In Figure 8, we show the pressure and friction coefficients predicted by AB-UPT for a normalized span location of $y/b = 0.5$ and compare it to the CFD simulation, showing that AB-UPT yields highly accurate predictions. We provide the same visualization for a different case with an angle-of-attack that is out of the training range ($\alpha = 20^\circ$) in Figure 9. Finally, we also show the 3D visualization of the corresponding wing including prediction error of the model in Figure 10.

E Data visualizations

In this section, we visualize several cases obtained by our numerical simulations. An important aspect when generating a dataset is quality control to ensure that all simulations have converged to meaningful solutions. Establishing convergence criteria for transonic wing simulations is challenging. We employed classical metrics including monitoring of residuals and force/moment coefficients on the wing. However, these indicators may not always distinguish between physically unsteady and/or discontinuous flows and numerical artifacts.

To supplement these conventional approaches, we employed AB-UPT as an additional quality control tool. The model’s prediction error served as an indicator of data quality—cases with anomalously high errors were flagged as potentially unconverged. This approach successfully identified failed cases where classical convergence monitors had been ambiguous. Manual inspection confirmed these cases exhibited spurious flow patterns, inadequate boundary layer mesh resolution, or early numerical

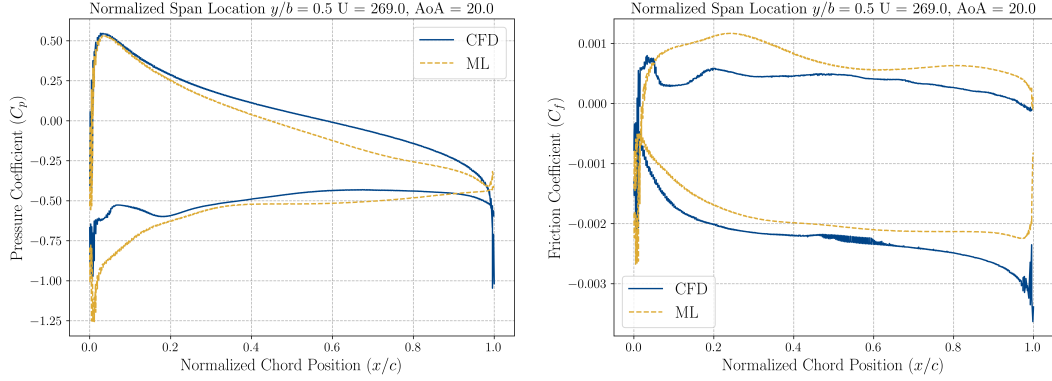


Figure 9: Comparison between CFD data (blue) and AB-UPT prediction (dashed yellow) for the pressure coefficient (C_p) and friction coefficient (C_f) on the wing surface at a normalized span location of $y/b = 0.5$ for a case of the parameter scans. 3D visualizations are shown Figure 10.

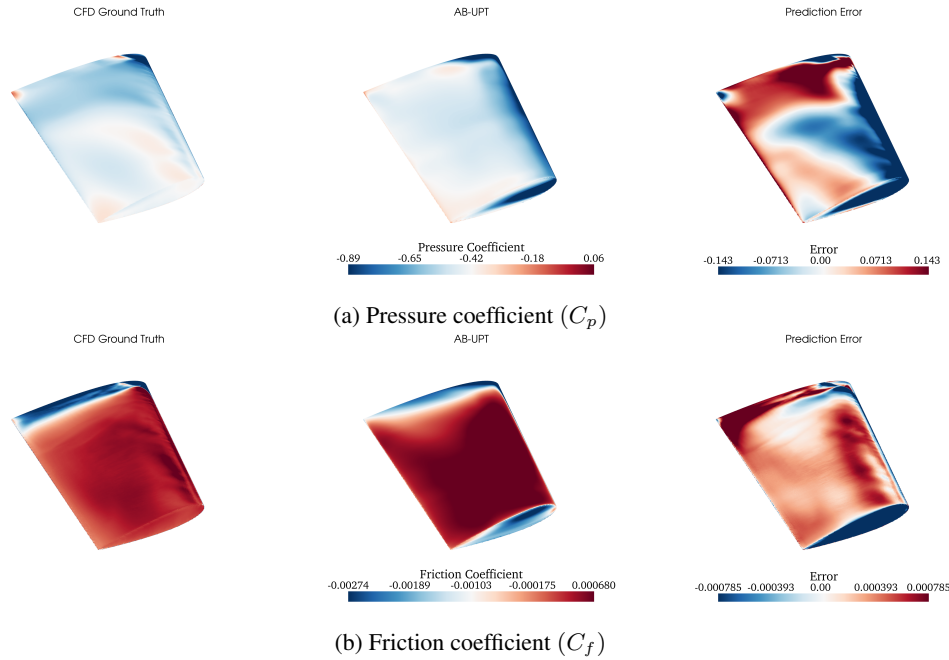


Figure 10: Comparison between surface field coefficients on the wing's surface of the CFD (left), AB-UPT surrogate (center) and the error between them (right). The case presented is from the parameter scan with $\Lambda = 40$ and $\alpha = 20$ far outside the training range. Corresponding surface pressure and friction profile plots are shown in Figure 9.

divergence (Figure 13). Removing these contaminated samples ensured the final dataset comprised numerically consistent solutions.

In Figure 14, we show the diversity of the dataset by visualizing the wing geometry and the corresponding surface pressure and volume velocity streamlines for various geometry parameters and inflow conditions.

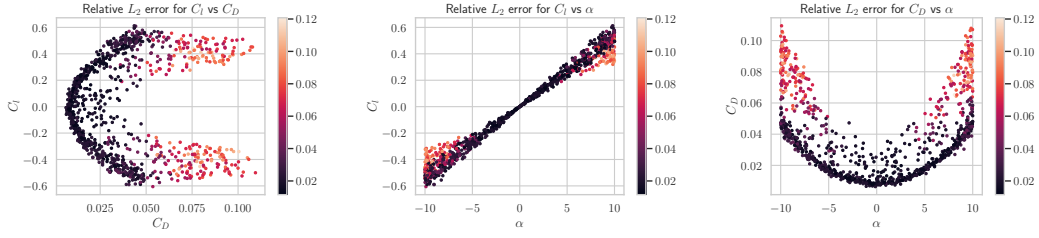


Figure 11: Distribution of relative L_2 error for C_D versus C_l (left), C_D versus α (middle), and C_l versus α (right) for the OOD test set. Most error is introduced in high C_D regimes, absent from the Pareto front.

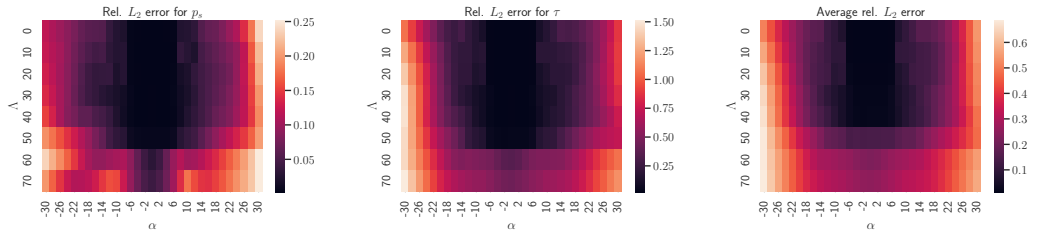


Figure 12: Relative L_2 error for p_s (left), τ (middle), and averaged over both (right) for parameter scans over α and Λ . AB-UPT is most error-prone at out-of-range values for $\Lambda \in \{60, 70\}$ and $\alpha \in \{-26, -28, -30\}$. For other out-of-range parameters AB-UPT is surprisingly stable.

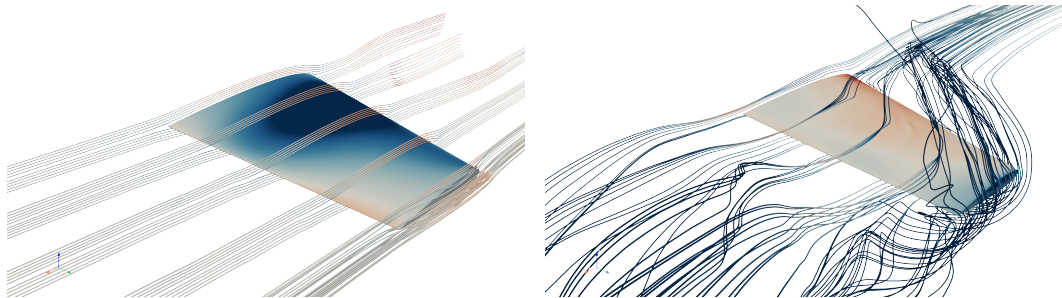


Figure 13: Illustration of failed cases caused by spanwise mesh quality variations (left) and numerically diverging case (right).

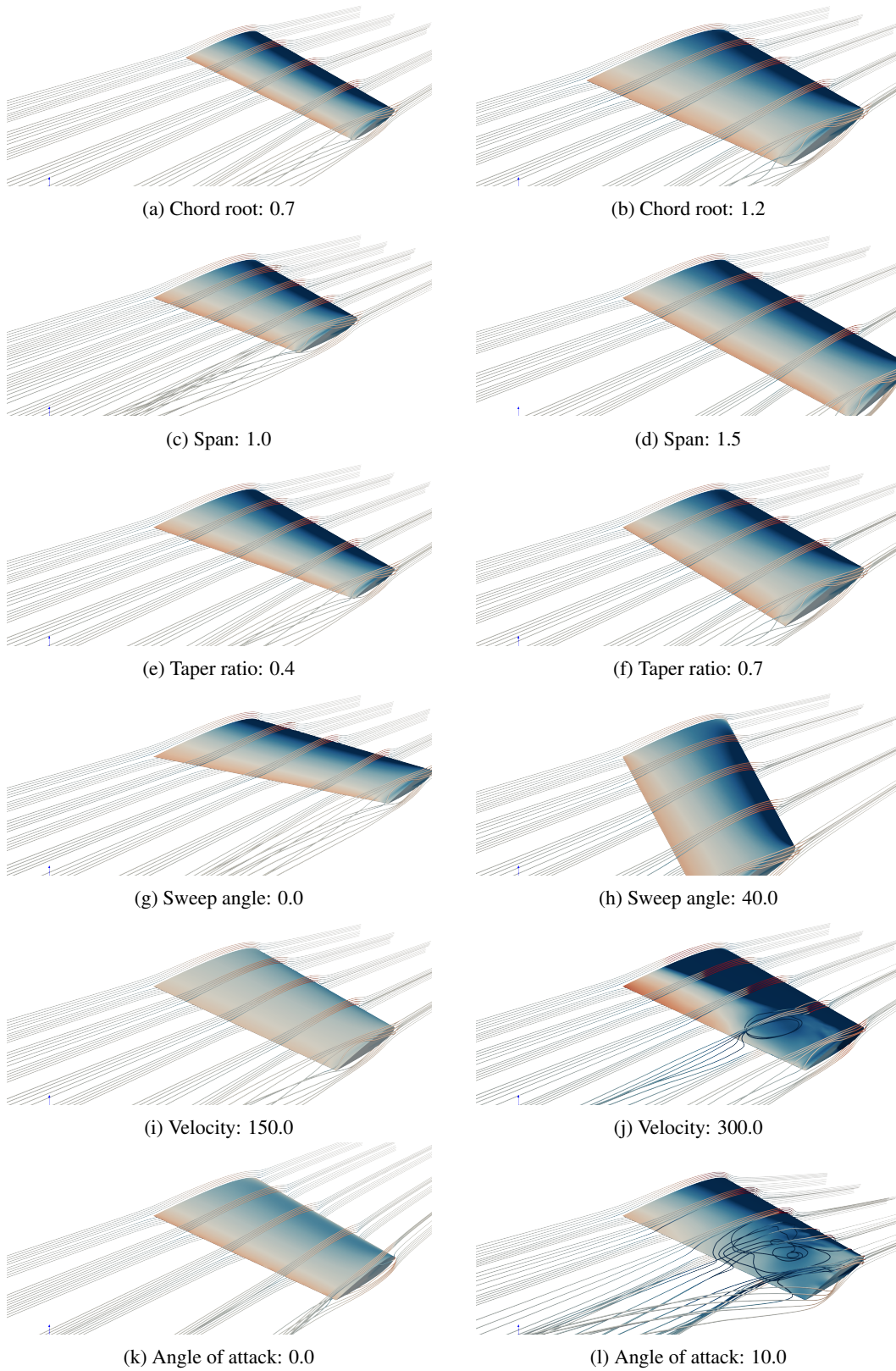


Figure 14: Wing geometry with corresponding surface pressure and volume velocity fields for various geometry design parameters and inflow conditions. In each row, the minimum and maximum values for each parameter are visualized, while all other parameters are set to their mean value. Except for k and l, the angle of attack shown is 4 degrees.